Radio-frequency thermal plasma-induced novel chainmail-like core-shell MoO$_2$ as highly stable catalyst for converting syngas to higher alcohols

Jianli Li[a], Ruijue Hu[b], Hao Qu[a], Yue Su[c], Na Wang[a], Haiquan Su[a,*], Xiaojun Gu[b,*]

[a] Inner Mongolia Key Laboratory of Chemistry and Physics of Rare Earth Materials, School of Chemistry and Chemical Engineering, Inner Mongolia University, Hohhot, 010021, China
[b] Inner Mongolia Key Laboratory of Coal Chemistry, School of Chemistry and Chemical Engineering, Inner Mongolia University, Hohhot, 010021, China
[c] School of Ecology and Environment, Inner Mongolia University, Hohhot, 010021, China

ABSTRACT

A novel core-shell catalyst with crystalline MoO$_2$ core and chainmail-like amorphous MoO$_X$ shell (noted as MoO$_2$-Pla) was prepared by radio-frequency induction thermal plasma method, and its catalytic performance for higher alcohols synthesis from syngas (CO and H$_2$) was compared with that of the MoO$_2$ catalysts synthesized by hydrothermal method and temperature programed reduction method (noted as MoO$_2$-Hyd and MoO$_2$-TPR). It was found that the chainmail-like shell formed under such extreme condition was both active to the reaction and inert to the thermal sintering, which was very fascinating and significantly different from those of the previous reported core-shell catalysts. The unusual amorphous species in the shell increased the CO conversion of MoO$_2$-Pla catalyst by 109 and 213.5%, respectively, compared with MoO$_2$-Hyd and MoO$_2$-TPR. More importantly, the shell formed under such ultra-high temperature (over 3000 °C) and ultra-fast quenching process exhibited ultra-stable chainmail-like particle surface, which endowed the catalyst with high catalytic stability within 300 h of experimental determination. This work provided a new alternative strategy and method for the design of high activity and high stability catalysts.

1. Introduction

In recent years, higher alcohols as a new kind of fuels have become more important and attracted much attention due to the increasing petroleum prices, environmental concerns and gasoline additive octane demands [1–4]. Moreover, higher alcohols are high value-added chemical products used in pharmaceutical industry, polyester industry and other chemical industries [5–8]. Thus, many researchers are devoted to the synthesis of higher alcohols from syngas (CO and H$_2$) [9], of which designing catalysts with high activity and stability is the key issue [10]. The catalysts for higher alcohols synthesis include modified Fischer-Tropsch catalysts [11], modified methanol synthesis catalysts [12], Rh-based catalysts [13,14] and Mo-based catalysts [15,16], among which Mo-based catalysts are more attractive because of their unique noble metal-like CO hydrogenation activity [16]. Although MoS$_2$- and Mo$_2$C-based catalysts show satisfactory activity, MoS$_2$ suffers from sulfide pollution [17] and Mo$_2$C is too expensive for industrial application [18]. MoO$_2$ catalysts exhibit better application prospect due to their low cost, easy preparation and excellent resistance to sulfur poisoning in catalytic process [18]. However, there are still many disadvantages

for MoO$_2$ catalysts such as low catalytic activity and higher alcohols selectivity, which restrict their large-scale applications [5,19,20]. There are many factors influencing the catalytic performance, such as the morphology and size [21–26], chemical compositions and reaction conditions [27,28] and the surface phases and species, among which the surface phases and species of catalyst are the most important factors influencing the catalytic performance and the reaction pathway [29–31]. In addition, the deactivation of catalyst, including the poisoning of active species, accumulation of carbonaceous species, agglomeration of catalysts, is still an important issue for the practical application [32,33].

Radio-frequency (RF) induction thermal plasma as a new technology can be used for the surface modification of materials, due to its high-energy ions and electrons, rapid heat transfer at ultra-high temperature (up to 10,000 °C), and the rapid cooling in the tail flame which can induce the formation of new and amorphous species on the material surface [34–38]. More importantly, the amorphous species have isotropic structures featuring much greater structural distortion and disorder, which can lead to high concentrations of unsaturated coordination sites, and subsequently the superior catalytic performance [39]. In

---

addition, the synergistic electron interaction between the new species on the catalyst surface and the bulk phases of catalyst could further improve the catalytic performance including activity, target selectivity and stability [29–31].

So far, catalysts with high activity used for higher alcohols synthesis under such harsh reaction conditions are easily sintering and deactivating, so it is an urgent issue to improve the stability and maintain the high activity of catalyst simultaneously. Thus, in this work, we proposed a new strategy to prepare a core-shell chainmail-like [40–42] MoO_2 catalyst by RF induction thermal plasma method and investigated its catalytic performance for higher alcohols synthesis from syngas at 300 °C and 9.0 MPa. In order to highlight the distinguishing features of MoO_2-Pla catalyst, another two reference catalysts were synthesized by hydrothermal method and temperature programed reduction method, respectively. From the results of transmission electron microscope (TEM), X-ray photoelectron spectra (XPS) and Raman spectra, it was found that the surface shell of MoO_2-Pla contained amorphous MoO_3 and Mo_4O_{11}, which were different from the surface species of MoO_2-Hyd and MoO_2-TPR, while the core phase of MoO_2-Pla was crystalline MoO_2. Interestingly, the MoO_2-Pla catalyst with amorphous surface species in the shell exhibited the remarkably enhanced catalytic performance including the CO conversion, the total alcohols selectivity and the higher alcohols selectivity, while the special shell produced at ultrahigh temperature showed outstanding thermal stability for anti-sintering.

2. Experimental

2.1. Chemicals

Ammonium heptamolybdate $((NH_4)_6Mo_7O_{24}\cdot4H_2O$, Tianjin Fengchuan Chemical Reagent Technologies Co., Ltd, > 99.0%), tartaric acid (HOOCCHOHCHOHCOOH, Tianjin Fengchuan Chemical Reagent Technologies Co., Ltd, > 99.0%) and potassium carbonate (K_2CO_3, Alfa Aesar, > 99.0%) were purchased without purification.

2.2. Catalysts preparation

The design and fabrication processes of MoO_2-Pla were illustrated in Fig. 1. The synthetic operation was carried out in a RF thermal plasma system under atmospheric pressure as shown in Fig. S1. The operation

Fig. 1. Schematic illustration of the rapid preparation process of MoO_2-Pla.

parameters of plasma for catalyst preparation were shown in Table S1. The experimental setup consists of an RF generator (12.0 kW) which is operated at the oscillating frequency of 8.0 MHz, a precursor powder supplier with a stirring device for feeding rate control, a quenching chamber, a gas allocating system, a powder-collecting filter at the bottom of the chamber and an exhaust system in the equipment. When the equipment was running, the raw material was added to the injection tube and blown into the plasma arc by the carrier gas. The cooling gas was blown for twenty minutes after the treatment.

$(NH_4)_6Mo_7O_{24}\cdot4H_2O$ was sieved to 80-mesh size and supplied into the plasma flame in a continuous way until the system reached a steady level and then the MoO_2-Pla catalyst was collected after the plasma was closed. For comparison, other two catalysts MoO_2-Hyd and MoO_2-TPR were synthesized. The synthetic procedures were as follows. $(NH_4)_6Mo_7O_{24}\cdot4H_2O$ (1.0 g) and tartaric acid (0.9 g, > 99.9%) were dissolved in deionized water. The pH value of the mixture solution was adjusted to 0.5 and then the solution was transferred into a Teflon-lined stainless steel autoclave. The MoO_2-Hyd was obtained after the hydrothermal reaction was performed at 180 °C for 24 h. For synthesis of MoO_2-TPR, $(NH_4)_6Mo_7O_{24}\cdot4H_2O$ (2.0 g) was placed in a tube furnace and heated at 550 °C for 5 h with a heating rate of 5 °C min^{-1} under H_2 atmosphere. In order to enhance synthesis efficiency of the higher alcohols, K_2CO_3 was added to the above three catalysts (MoO_2-Pla, MoO_2-Hyd and MoO_2-TPR) via impregnation method (5 wt%) before the catalytic performance was measured.

For revealing the influences of valence states of Mo on the catalytic performance, two MoO_3 catalysts were prepared using calcination and plasma method (noted as MoO_3-Cal and MoO_3-Pla), respectively. In detail, MoO_3-Cal was prepared by calcining $(NH_4)_6Mo_7O_{24}\cdot4H_2O$ (2.0 g) in a muffle furnace at 500 °C for 5 h with a heating rate of 5 °C min^{-1}, and MoO_3-Pla was prepared by plasma treatment using MoO_3-Cal as raw material.

2.3. Catalysts characterization

Transmission electron microscope images were obtained using a FEI Tecnai G2F20 TEM (200 KV). X-ray powder diffraction (XRD) patterns of the tested catalysts were obtained on a Panalytical X'pert Pro powder diffractometer using Cu Kα radiation operated at 40 kV and 40 mA. Specific surface analyses of the samples were obtained from the isotherms of nitrogen adsorption by means of an automatic volumetric device (Micromeritics ASAP 2020) using Brunauer–Emmett–Teller (BET) method. Raman spectra were recorded with a HORIBA SCIENTIFIC LabRAM HR Evolution spectrometer using a 514 nm line of semiconductor laser as the excitation source. H_2-TPR and CO-TPD measurements were performed on a Micromeritics AutoChem II 2920 apparatus equipped with a thermal conductivity detector (TCD). The fresh catalyst (0.08 g) was loaded in a U-tube quartz reactor and purged at Ar atmosphere for 0.5 h at 100 °C with heating rate of 10 °C min^{-1} and then cooled to 50 °C. For CO-TPD, after the pre-treatment, 5% CO/Ar was introduced to the reactor at 50 °C for 1 h and then the sample was heated to 900 °C by a rate of 10 °C min^{-1} under Ar stream. The desorbed CO was monitored by TCD. For H_2-TPR, after the pre-treatment, 10% H_2/Ar was introduced to the reactor and then the sample was heated to 900 °C by a rate of 10 °C min^{-1}. The XPS tests were conducted using an ESCALAB 250Xi photo electron spectrometer (Thermo Fisher Scientific).

2.4. Catalytic tests

The catalytic tests for higher alcohols synthesis were carried out at 9.0 MPa, 300 °C and 3000 h^{-1} in a fixed-bed micro-reactor (stainless steel, 520 mm length, 8 mm inside diameter). The analyses for catalytic products were performed on gas chromatography.
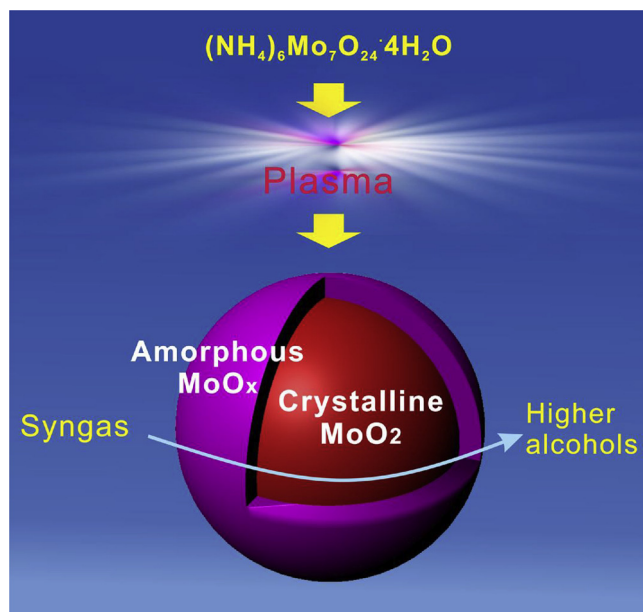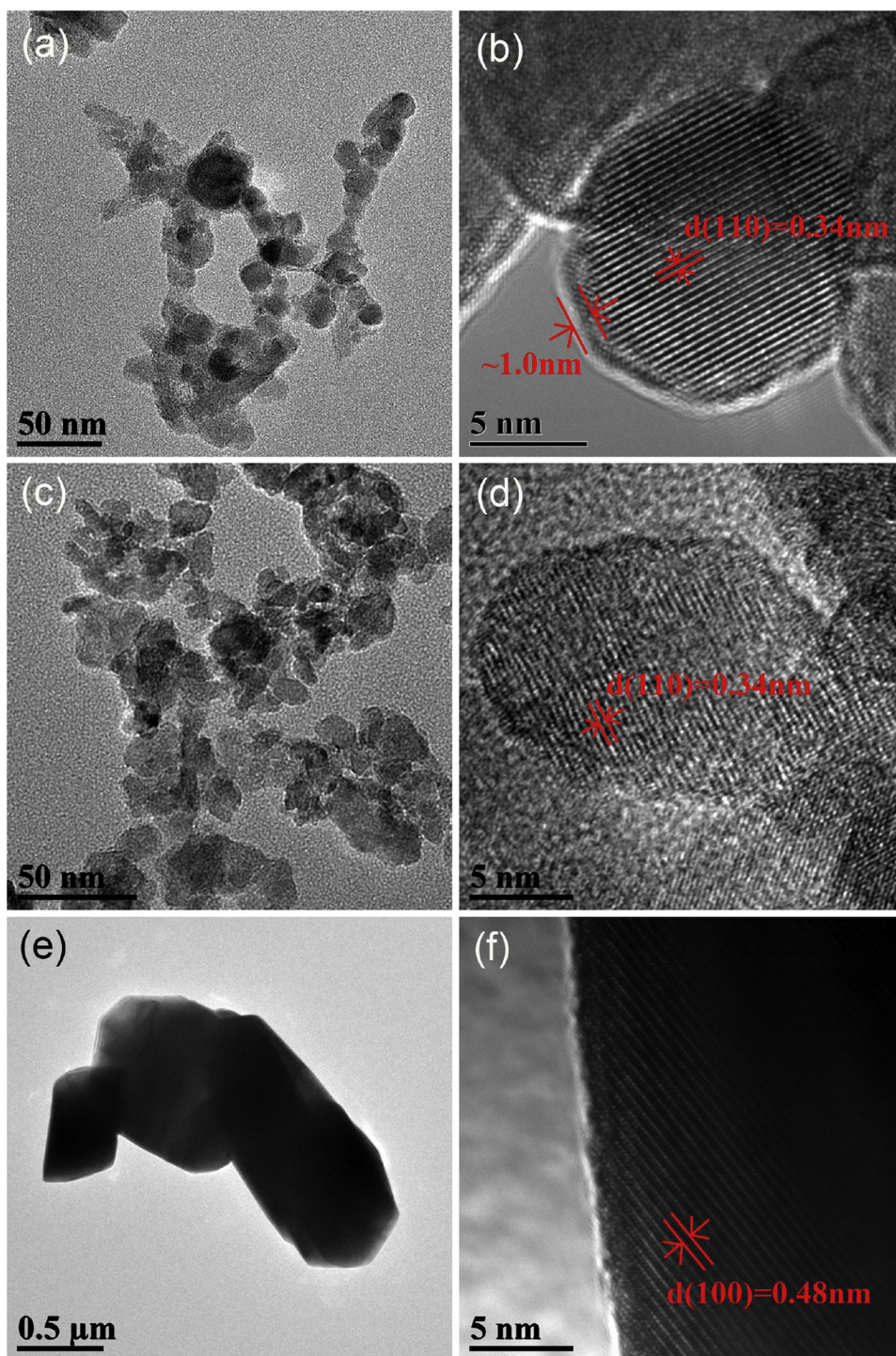
Fig. 2. TEM and HRTEM images of (a, b) MoO$_2$-Pla, (c, d) MoO$_2$-Hyd and (e, f) MoO$_2$-TPR.

3. Results and discussion

3.1. Catalyst characterization

Fig. 2a–f was the TEM images of three fresh catalysts. The particle size distributions of the three catalysts were also shown in Fig. S2 and the average particle sizes were 22.8, 19.2 and 647.3 nm, respectively (Table S2). It could be seen that MoO$_2$-Pla catalyst showed uniform spherical particles with a size of 15–20 nm and each particle exhibited a special core-shell structure (Fig. 2a and b). It should also be noted that the particles size of MoO$_2$-Hyd was similar to that of MoO$_2$-Pla.

However, the MoO$_2$-TPR catalyst exhibited a size of 300–600 nm, which was far larger than the previous two. The interplanar crystal spacings of bulk phases of MoO$_2$-Pla, MoO$_2$-Hyd and MoO$_2$-TPR were measured to be 0.34, 0.34 and 0.48 nm (Fig. 2b, d and f), corresponding to the (110), (110) and (100) planes of MoO$_2$, respectively [43]. It was surprising that a uniform surface shell with thickness of about 1.0 nm without lattice fringe was observed unexpectedly on the surface of MoO$_2$-Pla, providing solid evidence that the surface species were amorphous. However, no core-shell structure was observed for MoO$_2$-Hyd and MoO$_2$-TPR catalysts. As is reported, the amorphous species have isotropic structures featuring much greater structural distortion and
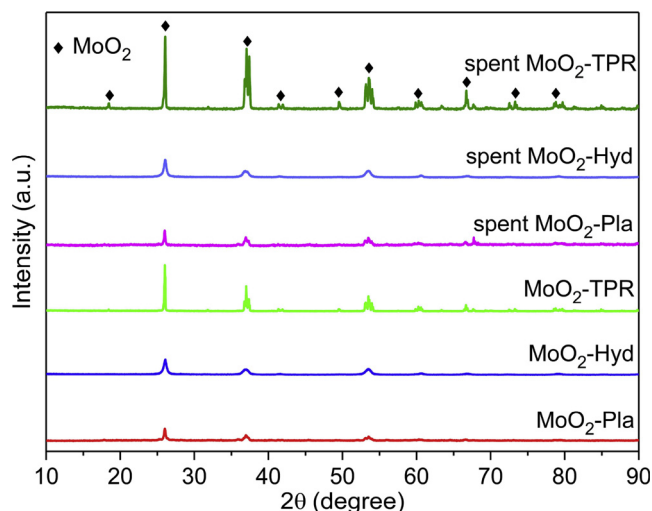
Fig. 3. XRD patterns of fresh and spent MoO_2 catalysts prepared by different methods.

Fig. 4. Raman spectra of MoO_2 catalysts prepared by different methods.

disorder, which is favorable for exposing more unsaturated coordination sites, which subsequently can lead to the superior catalytic performance [39].

For investigating the structure of the catalysts, XRD was employed to analyze the phase composition. It was found that the diffraction peaks appeared at 26.0, 37.0, 41.3, 49.5, 53.1, 60.6, 66.7, 73.2 and 78.8° (Fig. 3) for three fresh MoO_2 catalysts (MoO_2-Pla, MoO_2-Hyd and MoO_2-TPR) and the corresponding spent catalysts could be assigned to the phase of monoclinic MoO_2 (PDF#:73-1249) [44,45]. The crystallite sizes of fresh MoO_2-Pla, MoO_2-Hyd, MoO_2-TPR, and spent MoO_2-Pla, MoO_2-Hyd and MoO_2-TPR calculated by Scherrer formula were 19.5, 17.4, 76.2, and 21.2, 19.8 and 92.8 nm, respectively (Table S2). The size increment for three catalysts MoO_2-Pla, MoO_2-Hyd and MoO_2-TPR was 1.7, 2.4 and 16.6 nm respectively after 300 h of reaction (the corresponding value was 2.8, 4.9 and 27.1 nm if the calculation was based on TEM results). It was clearly found that the MoO_2-Pla had the minimum size increment, indicating that MoO_2-Pla active particles had the capacity to prevent themselves from aggregating. In other words, the shell of the MoO_2-Pla particles was physically inert and these particles were armored to prevent themselves from thermal sintering and agglomerating.

The specific surface area of the three catalysts MoO_2-Pla, MoO_2-Hyd and MoO_2-TPR calculated using BET method were 44.7, 35.4 and 1.5 $m^2 g^{-1}$, respectively (Table S3). The average particle sizes from TEM statistics of the three catalysts were 22.8, 19.2 and 647.3 nm, respectively. The rather low specific surface area of MoO_2-TPR could be owing to the huge particle size. The specific surface area of MoO_2-Pla was bigger than that of MoO_2-Hyd even though the former had bigger particle size. This is because the amorphous surface of MoO_2-Pla is also contributed to the specific surface area [46–48]. The greater dispersion of MoO_2-Pla from TEM results could also increase its specific surface area. The active site at catalyst surface was tightly associated with the specific surface area, and the catalyst MoO_2-Pla with higher specific surface area was likely to show better catalytic activity than the other two catalysts.

Since the XRD technique could not identify the species on the catalyst surface, the Raman spectroscopy was used to perform the characterizations. The results of Raman spectra showed that the surface species of MoO_2-Pla were MoO_3 and Mo_4O_{11} and the surface species of MoO_2-Hyd was MoO_3, while the surface species of MoO_2-TPR were MoO_2, MoO_3 and Mo_4O_{11} (Fig. 4) [49]. Combined with the XRD and TEM results, we could know that the surface species of the amorphous shell of MoO_2-Pla were MoO_3 and Mo_4O_{11}. These different surface species might make different contributions to the catalytic performance
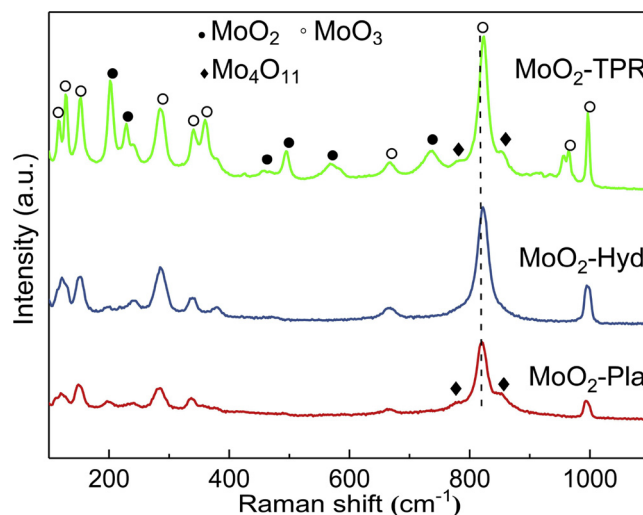
for higher alcohols synthesis. The different full width at half maxim (FWHM) of the peak at around 823 cm^{-1} for the three catalysts MoO_2-Pla, MoO_2-Hyd and MoO_2-TPR was 23.4, 18.9 and 16.3 cm^{-1} respectively, demonstrating that the surface species of MoO_2-Pla had the poorest crystallinity among the three samples, which coincided with the TEM results. Moreover, the Raman peak at 823 cm^{-1} shifted to the lower wavenumber in MoO_2-Pla, indicating that the electron density [50] between Mo atom and O atom on the surface of MoO_2-Pla was lower than that of MoO_2-Hyd and MoO_2-TPR. This decreased electron density was caused by the strong interaction between bulk MoO_2 and surface species, and it should relate to the adsorbtion behaviour of CO molecules in syngas on the surface of catalysts, which subsequently influenced the product selectivity.

The H_2-TPR experiments of three samples were performed to study the reduction behaviors of MoO_2 nanoparticles, which was further used to evaluate the interaction between the surface species and the bulk MoO_2. As shown in Fig. 5a, the peaks at low temperature region (400–600 °C) could be attributed to the reduction of MoO_3 and Mo_4O_{11} to MoO_2, while the peaks at high temperature region (600–900 °C) were assigned to the reduction of MoO_2 to Mo [45,51–53]. The intensity of the peak at about 532 °C for MoO_2-Pla was far stronger than that of the peaks at about 446 and 517 °C for other two samples, indicating that the content of the surface MoO_3 and Mo_4O_{11} was the highest and lowest on MoO_2-Pla and MoO_2-TPR, respectively. The reduction temperatures of MoO_2-TPR were higher than that of MoO_2-Hyd, which could be due to the different particle size [54,55]. Surprisingly, the reduction temperatures of MoO_2-Pla were significantly higher than that of MoO_2-Hyd at similar particle size. This result could be attributed to the strong interaction between the surface high valent species and the bulk MoO_2, which was consistent with the Raman analysis. It should be noted that at high temperature region, MoO_2-Pla exhibited two peaks at 763 and 837 °C, while the other two samples had only one peak. This might be due to that the reduced amorphous MoO_2 and the bulk MoO_2 in MoO_2-Pla had different reduction temperatures. Also, half of the peak area at 763 °C was larger than the whole peak area at 532 °C, indicating that some bulk MoO_2 was influenced by the surface species and was also reduced at 763 °C, which further suggested the strong interaction between the surface high valent species and the bulk MoO_2.

Due to the close correlation between the catalytic activity and the adsorption/desorption behavior of reactants, the CO-TPD tests of MoO_2-Pla, MoO_2-Hyd and MoO_2-TPR were carried out. Two types of CO desorption peaks at different temperatures were observed for the three catalysts (Fig. 5b). One was the low temperature desorption peak at around 300 °C, corresponding to the non-dissociative adsorption of CO; another was the high temperature desorption peak at about 400–500 °C,
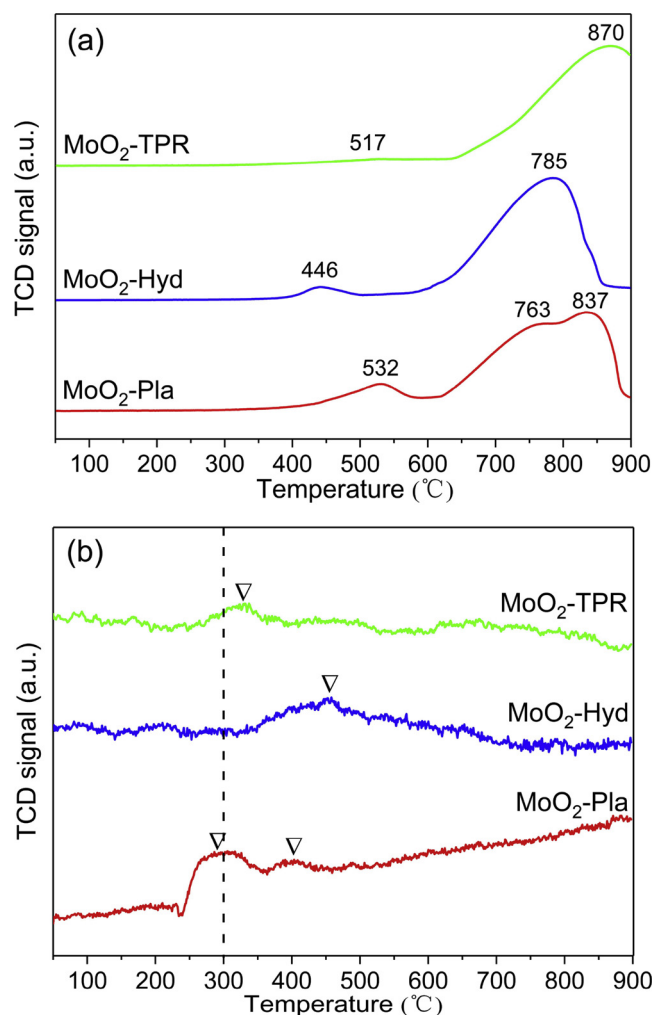
Fig. 5. (a) H_2-TPR profiles of MoO_2 catalysts prepared by different methods; (b) CO-TPD profiles of MoO_2 catalysts prepared by different methods.

relating to the dissociative adsorption of CO. It could be seen that only MoO_2-Pla had the strongest desorption peak among the three samples, suggesting that this catalyst surface had more adsorption/desorption sites as was confirmed by the BET analyses, which was beneficial for the catalytic activity [56]. The same amount of K_2CO_3 was added to the three catalysts, and we could expect a fairly high ratio between K_2CO_3 and the surface MoO_x active sites for MoO_2-TPR duo to its huge size and low specific surface area. The excessive K_2CO_3 of MoO_2-TPR would cover the active sites and might lead to the poorer adsorption capacity for CO. Generally speaking, higher alcohols are formed by the synergistic effect of two or more kinds of active centers. Some of these active centers are dissociative adsorption centers and some are non-dissociative adsorption centers. Only the proper proportion of these two centers can guarantee the high yield of higher alcohols. The special properties such as the unusual electron transfer between the core and the shell and lower electron density of the surface species of MoO_2-Pla greatly promoted the adsorption and activation for CO, and also made the ratio of dissociative adsorption center and non-dissociative adsorption center optimized. Thus, catalyst MoO_2-Pla had more balanced dissociative/non-dissociative adsorption sites, which would be favorable for improving the total alcohols selectivity and the higher alcohols selectivity in the reaction process.

In order to further understand the surface characteristics of catalysts, we carried out the XPS measurements. From the XPS spectra of MoO_2-Pla, MoO_2-Hyd and MoO_2-TPR (Fig. 6), it was observed that all the catalysts exhibited Mo^{6+} and Mo^{5+} two oxidation states besides
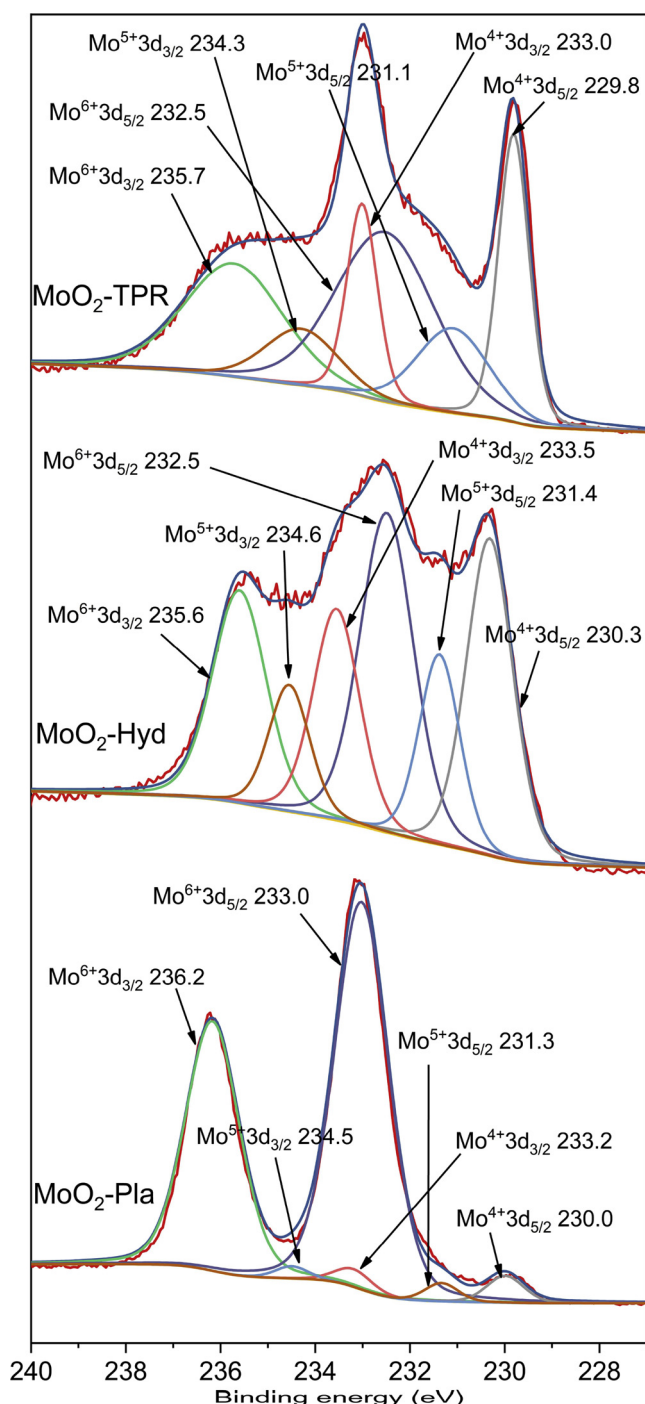

Fig. 6. XPS spectra of Mo 3d of the MoO_2 catalysts prepared by different methods.

Mo^{4+} [44,57,58]. Table S4 summarized the results of the peak positions and the percentages of Mo species calculated on the basis of peak areas. The binding energy of Mo^{6+} of MoO_2-Pla was obviously shifted to a higher value compared with the other two catalysts, which indicated that the electron density of the surface species MoO_3 of MoO_2-Pla was lower than that of others, which was consistent with the Raman spectra results and H_2-TPR analyses. It was evident that there was a special interaction between the surface species and bulk MoO_2 in MoO_2-Pla catalyst, which influenced the electron density of the surface species. The surface element content calculated from XPS was shown in Table S5. The carbon content of three fresh catalysts MoO_2-Pla, MoO_2-Hyd and MoO_2-TPR were 12.5%, 17.8% and 11.7% respectively, which

could be considered as the pollution in the air. After the reaction, the carbon content of the corresponding spent catalysts became 47.9%, 64.4% and 73.1% respectively, suggesting that a large amount of carbon deposition was formed during the catalytic reaction. Obviously, the carbon content of MoO_2-Pla was the lowest, implicating that this catalyst might had the best catalytic stability [59]. Meanwhile, the rather high carbon content of MoO_2-TPR also caused the intensity decline of Mo3d signal in XPS of the spent catalyst (Fig. S5). In addition, the ratio of K and Mo was listed in Table S5. These ratios for MoO_2-Pla and MoO_2-Hyd were similar while that for MoO_2-TPR was rather high. The excessive K species would cover the active sites, which led to poor catalytic performance. There was no obvious change for K/Mo ratio after the reaction, indicating that there was no obvious K loss.

3.2. Catalytic performance

For exploring the role of different surface phases and species of MoO_2 catalysts in converting syngas to higher alcohols, the catalytic performance of MoO_2-Pla, MoO_2-Hyd and MoO_2-TPR catalysts was measured. The results showed that among the three catalysts, MoO_2-Pla had the highest CO conversion, total alcohols selectivity, $C_{2+}OH$ distribution and STY of total alcohols, which reached 16.3%, 45.6%, 77.6%, 59.1 mg g^{-1} h^{-1}, respectively (Fig. 7, Table S6). Also, it had the lowest selectivity of hydrocarbons.

The catalytic activity with time on stream of 300 h of the three catalysts was also investigated. It was found that the catalytic performance of MoO_2-Hyd and MoO_2-TPR decreased with time, while that of MoO_2-Pla almost had no decrease except $C_{2+}OH$ selectivity (Fig. 8). This ultra-stable performance was very eye-catching in the research field of higher alcohols synthesis.

3.3. Role of novel chainmail-like core-shell structure

Interestingly, for the MoO_2 catalyst with novel chainmail-like core-shell structure, the shell had rich speices and was chemically active but physycally inert, while the core had strong interaction with the shell. The comparison of catalytic performance of MoO_2-Pla and MoO_2-Hyd indicated that the catalyst synsesized via plasma technique distinctly enhanced its catalytic performance by generating unusual amorphous species on the shell of core-shell structure. As mentioned above, the amorphous species are favorable for exposing more unsaturated coordination sites, i.e. the catalytic active sites [39]. Also, the amorphous composition could provide more surface areas (BET) and defects to adsorb reactant molecules [22,23]. By comparing the catalytic performance and particle size of MoO_2-Hyd and MoO_2-TPR, we could further understand that the small particle size could also improve the catalytic performance through exposing more active surface [24,25]. Thus, the amorphous surface species and the ultra-small particles endowed MoO_2-Pla more specific surface area and active sites than MoO_2-Hyd and MoO_2-TPR, as was revealed by TPD analyses.

As discussed earlier, the special core-shell structure of MoO_2-Pla produced strong synergistic interaction between the surface species and the bulk MoO_2, which resulted in an unusual electron transfer between the core and the shell and a lower electron density of the surface species MoO_3 on this catalyst. The electron-deficient areas on the shell might accept electrons from the adsorbed molecules, interact with the lone pair electrons, participate in σ-bonding with the adsorbed CO, reduce the adsorption energy of intermediates and reduce the repulsion to facilitate CO insertion [60–63]. These properties greatly promoted the adsorption and activation of MoO_2-Pla for CO, and offered catalyst MoO_2-Pla more balanced dissociative/non-dissociative adsorption sites (Fig. 5b). Usually, higher alcohols were formed by the synergistic effect of two or more kinds of active centers [64], thus these balanced active sites might make a significant promotion on the surface chemical properties of catalysts [65–68] and would be favorable for improving the total alcohols selectivity and the higher alcohols selectivity.

The change of surface species in the shell is another factor to influence the catalytic performance. In order to verify the surface species change with reaction time, the in-situ Raman spectra of MoO_2-Pla were carried out using syngas under atmospheric pressure at 300 ˚C. Obviously, with the increase of reaction time, the peak of MoO_3 became weaker (Fig. 9). Through fitting the peaks, the percentage of the peak area at 823 cm^{-1} in the total area was 6.64, 5.97, 2.73 and 0%, respectively. This indicated that the MoO_3 was gradually reduced under the reducing atmosphere, which was consistent with the XPS results. In addition, compared with the fresh MoO_2-Pla, the spent MoO_2-Pla had the decreased percentage of Mo^{6+} ions (Fig. S5 and Table S4). Normally, the in-situ produced intermidiates could exhibit more active sites [69,70]. That is, more active sites could be produced with the ruduction of MoO_3 with time. Thus, the whole catalytic performance such as the CO conversion, STY of total alcohols and $C_{2+}OH$ and total alcohols selectivity significantly increased with time. On the other hand, a gradual decline of the surface species MoO_3 led to a decrease of a particular type of active centers in catalyst, which deteriorated the balanced catalytic active centers, thus resulted in the decreased $C_{2+}OH$ selectivity and the increase amount of methanol (Fig. 8e).

3.4. Role of radio-frequency thermal plasma

Various efforts have been made to study the relationship between catalytic performance and structural properties such as composition phases, crystal planes, morphology and size [21–26,71]. The MoO_2-Pla catalyst prepared using thermal plasma technique featured core-shell structure, small size, amorphous chainmail-like shell, strong core-shell interaction and rich surface species, leading to larger surface area, more
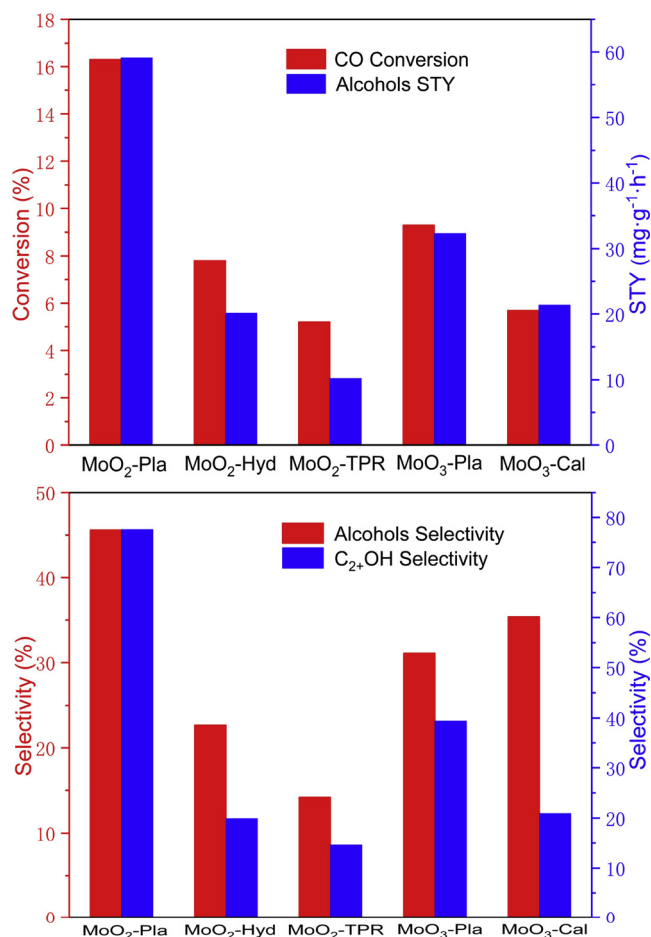

Fig. 7. Catalytic performance of the MoO_2 and MoO_3 catalysts for higher alcohols synthesis.
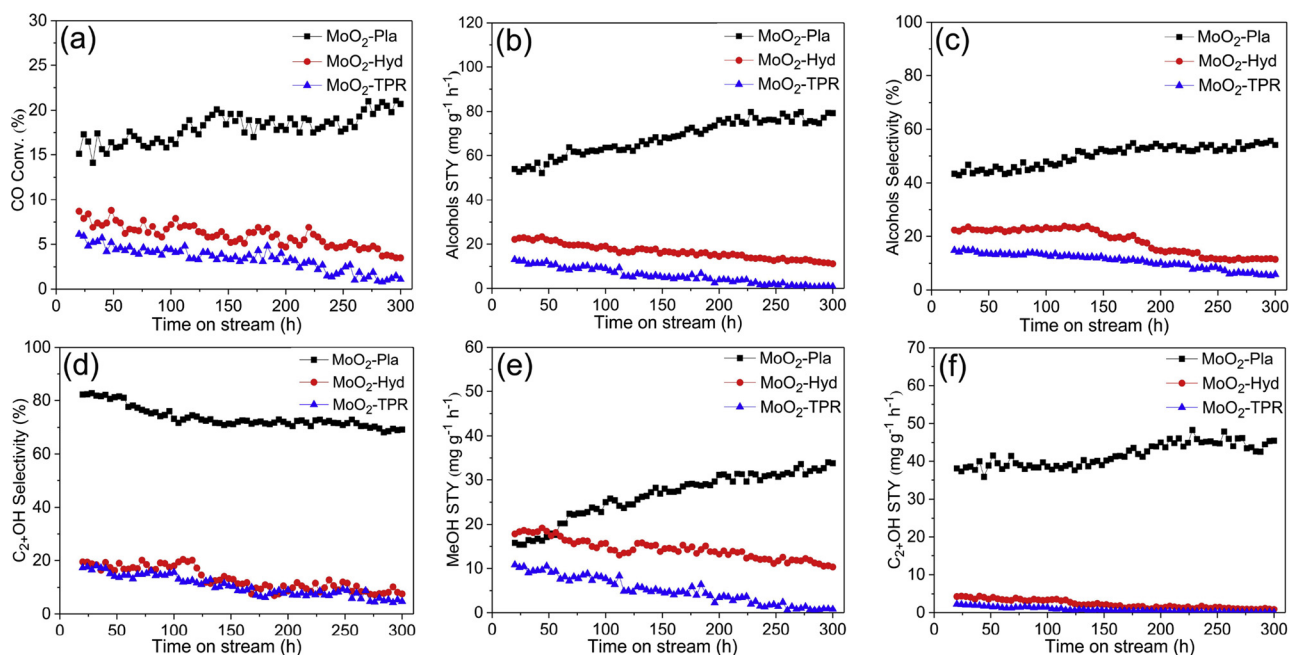
Fig. 8. Plots of the catalytic performance against time on stream for (a) CO conversion, (b) alcohols STY, (c) alcohols selectivity, (d) $C_{2+}OH$ selectivity, (e) MeOH STY and (f) $C_{2+}OH$ STY.
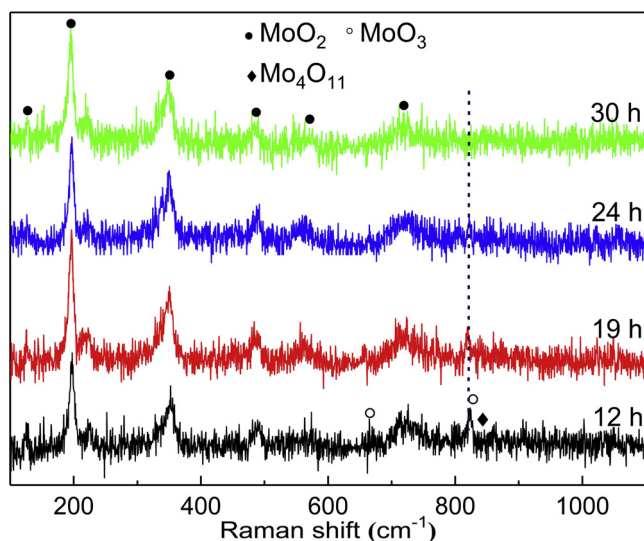

Fig. 9. In-situ Raman spectra of MoO_2-Pla at different reaction time.

catalytic active sites and balanced active site type, which further resulted in high catalytic performance on the higher alcohols synthesis. In order to further verify the effect of plasma treatment on catalytic performance, MoO_3-Cal and MoO_3-Pla catalysts were also prepared and studied. Fig. S3 obviously illustrated that the particle size of MoO_3-Pla was much smaller than that of MoO_3-Cal. We could also see that the surface of MoO_3-Pla had 5 nm thick amorphous phase while that of MoO_3-Cal had not. The catalytic results (Fig. 7, Table S6) clearly demonstrated that the catalytic performance of MoO_3-Cal was rather poor, while the catalytic performance of MoO_3-Pla, especially the $C_{2+}OH$ distribution and STY of total alcohols, increased obviously. From the TEM results of the spent catalysts (Fig. S4), we could find that the particle size of spent MoO_2-Pla almost did not change but the spent MoO_2-Hyd and MoO_2-TPR exhibited obvious aggregation. The average particle size of three fresh catalysts MoO_2-Pla, MoO_2-Hyd and MoO_2-TPR from TEM statistics was 22.8, 19.2, 647.3 nm, respectively, and that of the corresponding spent catalysts was 25.6, 24.1, 674.4 nm,

respectively (Fig. S2, Table S2). These results clearly evidenced that MoO_2-Pla had the minimum size increasement (2.8 vs 4.9 and 27.1 nm) and the shell endowed the catalyst high catalytic stability. It should be noted that the surface amorphous shell of MoO_2-Pla had not disappeared after reaction, which indicated that the core-shell structure of the particles produced by thermal plasma was fairly stable under high temperature and pressure. From the XPS results of the spent cataltsts (Fig. S5, Table S4), we could see that there was no obvious binding energy shift for the spent MoO_2-Pla unlike for the fresh sample. This difference could be explained by the different formation conditions of surface Mo^{6+} for the spent MoO_2-Pla and the fresh MoO_2-Pla. The surface Mo^{6+} species of the three fresh samples were formed during different preparation process via plasma, hydrothermal and TPR methods, respectively, which resulted in the different chemical environment around Mo^{6+} for different fresh samples. Thus, the binding energy shift was observed among the three fresh samples. However, the Mo^{6+} species on the surface of spent samples were formed by oxidizing the low covalent Mo species when exposing the samples to atmosphere after the reaction, which resulted in the identical chemical environment around Mo^{6+} for different spent samples. Thus, no binding energy shift was observed among the three spent samples. It should also be pointed out that the low covalent Mo species were produced by the reduction of Mo^{6+} during the catalytic reaction process, which was confirmed by Raman results. These results further proved that the electronic distribuition state of MoO_2-Pla produced by plasma was rather special compared with the other two catalysts. Also, the carbon content of spent MoO_2-Pla was obviously lower than spent MoO_2-Hyd and MoO_2-TPR (Table S5), indicating that the plasma environment endowed MoO_2-Pla with the ability of anti-carbon deposition. The ultrafast quenching process and super-high temperature under thermal plasma conditions resulted in an unusual chainmail-like shell, which could efficiently prevent the catalyst particles from aggregating, leading to the stable catalytic performance. In summary, thermal plasma treatment could efficiently modify the surface structure and electronic property of catalysts and consequently improve their catalytic performance.

4. Conclusions

In conclusion, a novel core-shell chainmail-like MoO_2 catalyst was

prepared by the RF induction thermal plasma method, and was used to catalyze higher alcohols synthesis from syngas. Compared with the MoO$_2$ catalysts prepared by other methods, the plasma-induced MoO$_2$ catalyst greatly increased the catalytic performance including CO conversion, C$_{2+}$OH selectivity, STY and thermal stability. The MoO$_2$-Pla catalyst prepared using thermal plasma technique featured core-shell structure, small particle size, amorphous chainmail-like shell, crystalline core, strong core-shell interaction, and rich surface species in the shell. The small size particles, together with the amorphous phase and rich speices in the shell made the MoO$_2$-Pla particles chemically active and offered more active sites for the enhanced catalytic activity. However, the strong interaction between the surface species in the shell and the crystalline MoO$_2$ in the core resulted in electron-deficient state on the shell, which subsequently influenced the balance of different adsorption sites and thus the total alcohols selectivity and the higher alcohols selectivity. The ultrafast quenching process and super-high temperature under thermal plasma conditions made the MoO$_2$-Pla particles physycally inert, just like a chainmail, which could efficiently prevent the catalyst particles from aggregating, leading to ultra-high long-term runing stability. Thus, thermal plasma treatment could efficiently modify the surface structure and electronic property of catalysts and consequently improve their catalytic performance. These findings suggested that through producing special structure and species on the surface of catalyst by RF induction thermal plasma, it may provide a possible avenue to develop highly efficient and stable catalysts for various applications.

Acknowledgements

Appendix A. Supplementary data

Supplementary material related to this article can be found, in the online version, at doi:https://doi.org/10.1016/j.apcatb.2019.02.060.

References

[1] S. Atsumi, T. Hanai, J.C. Liao, Non-fermentative pathways for synthesis of branched-chain higher alcohols as biofuels, Nature 451 (2008) 86–89.

[2] J.J. Spivey, A. Egbebi, Heterogeneous catalytic synthesis of ethanol from biomass-derived syngas, Chem. Soc. Rev. 36 (2007) 1514–1528.

[3] J. Goldemberg, Ethanol for a sustainable energy future, Science 315 (2007) 808–810.

[4] Z. He, Q. Qian, J. Ma, Q. Meng, H. Zhou, J. Song, Z. Liu, B. Han, Water-enhanced synthesis of higher alcohols from CO$_2$ hydrogenation over a Pt/Co$_3$O$_4$ catalyst under milder conditions, Angew. Chem. Int. Ed. 55 (2016) 737–741.

[5] H.T. Luk, C. Mondelli, D.C. Ferré, J.A. Stewart, J. Pérez-Ramírez, Status and prospects in higher alcohols synthesis from syngas, Chem. Soc. Rev. 46 (2017) 1358–1426.

[6] Z. An, X. Ning, J. He, Ga-promoted CO insertion and C-C coupling on Co catalysts for the synthesis of ethanol and higher alcohols from syngas, J. Catal. 356 (2017) 157–164.

[7] G. Prieto, S. Beijer, M.L. Smith, M. He, Y. Au, Z. Wang, D.A. Bruce, K.P. de Jong, J.J. Spivey, P.E. de Jongh, Design and synthesis of copper-cobalt catalysts for the selective conversion of synthesis gas to ethanol and higher alcohols, Angew. Chem. Int. Ed. 53 (2014) 6397–6401.

[8] J. Qi, N. Benipal, C. Liang, W. Li, PdAg/CNT catalyzed alcohol oxidation reaction for high-performance anion exchange membrane direct alcohol fuel cell (alcohol = methanol, ethanol, ethylene glycol and glycerol), Appl. Catal. B: Environ. 199 (2016) 494–503.

[9] Y. Lu, R. Zhang, B. Cao, B. Ge, F.F. Tao, J. Shan, L. Nguyen, Z. Bao, T. Wu, J.W. Pote, B. Wang, F. Yu, Elucidating the copper-hägg iron carbide synergistic interactions for selective CO hydrogenation to higher alcohols, ACS Catal. 7 (2017) 5500–5512.

[10] S. Gao, X. Li, Y. Li, H. Yu, F. Zhang, Y. Sun, H. Fang, X. Zhang, X. Liang, Y. Yuan, Effects of gallium as an additive on activated carbon-supported cobalt catalysts for the synthesis of higher alcohols from syngas, Fuel 230 (2018) 194–201.

[11] Y. Xiang, R. Barbosa, X. Li, N. Kruse, Ternary cobalt-copper-niobium catalysts for the selective CO hydrogenation to higher alcohols, ACS Catal. 5 (2015) 2929–2934.

[12] J. Sun, Q. Cai, Y. Wan, S. Wan, L. Wang, J. Lin, D. Mei, Y. Wang, Promotional effects of cesium promoter on higher alcohol synthesis from syngas over cesium-promoted Cu/ZnO/Al$_2$O$_3$ catalysts, ACS Catal. 6 (2016) 5771–5785.

[13] X. Pan, Z. Fan, W. Chen, Y. Ding, H. Luo, X. Bao, Enhanced ethanol production inside carbon-nanotube reactors containing catalytic particles, Nat. Mater. 6 (2007) 507–511.

[14] J. Liu, Z. Guo, D. Childers, N. Schweitzer, C.L. Marshall, R.F. Klie, J.T. Miller, R.J. Meyer, Correlating the degree of metal-promoter interaction to ethanol selectivity over MnRh/CNTs CO hydrogenation catalysts, J. Catal. 313 (2014) 149–158.

[15] E.T. Liakakou, E. Heracleous, K.S. Triantafyllidis, A.A. Lemonidou, K-promoted NiMo catalysts supported on activated carbon for the hydrogenation reaction of CO to higher alcohols: Effect of support and active metal, Appl. Catal. B: Environ. 165 (2015) 296–305.

[16] S. Zaman, K.J. Smith, A review of molybdenum catalysts for synthesis gas conversion to alcohols: catalysts, mechanisms and kinetics, Catal. Rev. 54 (2012) 41–132.

[17] J.E. Hensley, S. Pylypenko, D.A. Ruddy, Deactivation and stability of K-CoMoS$_x$ mixed alcohol synthesis catalysts, J. Catal. 309 (2014) 199–208.

[18] S.K. Bej, C.A. Bennett, L.T. Thompson, Acid and base characteristics of molybdenum carbide catalysts, Appl. Catal. A Gen. 250 (2003) 197–208.

[19] C.-H. Ma, H.-Y. Li, G.-D. Lin, H.-B. Zhang, Ni-decorated carbon nanotube-promoted Ni–Mo–K catalyst for highly efficient synthesis of higher alcohols from syngas, Appl. Catal. B: Environ. 100 (2010) 245–253.

[20] H.T. Luk, T. Forster, C. Mondelli, S. Siol, D. Curulla-Ferré, J.A. Stewart, J. Pérez-Ramírez, Carbon nanofibres-supported KCoMo catalysts for syngas conversion into higher alcohols, Catal. Sci. Technol. 8 (2018) 187–200.

[21] D. Geng, H. Wang, G. Yu, Graphene single crystals: size and morphology engineering, Adv. Mater. 27 (2015) 2821–2837.

[22] S. Najafishirtari, C. Guglieri, A. Marras, A. Scarpellini, R. Brescia, M. Prato, G. Righi, A. Franchini, R. Magri, L. Manna, M. Colombo, Metal-support interaction in catalysis: the influence of the morphology of a nano-oxide domain on catalytic activity, Appl. Catal. B: Environ. 237 (2018) 753–762.

[23] C. Dong, Z. Ma, R. Qie, X. Guo, C. Li, R. Wang, Y. Shi, B. Dai, X. Jia, Morphology and defects regulation of carbon nitride by hydrochloric acid to boost visible light absorption and photocatalytic activity, Appl. Catal. B: Environ. 217 (2017) 629–636.

[24] J. Carbajo, A. Tolosana-Moranchel, J.A. Casas, M. Faraldos, A. Bahamonde, Analysis of photoefficiency in TiO$_2$ aqueous suspensions: effect of titania hydrodynamic particle size and catalyst loading on their optical properties, Appl. Catal. B: Environ. 221 (2018) 1–8.

[25] Z. Wei, L. Rosa, K. Wang, M. Endo, S. Juodkazis, B. Ohtani, E. Kowalska, Size-controlled gold nanoparticles on octahedral anatase particles as efficient plasmonic photocatalyst, Appl. Catal. B: Environ. 206 (2017) 393–405.

[26] R. Peng, S. Li, X. Sun, Q. Ren, L. Chen, M. Fu, J. Wu, D. Ye, Size effect of Pt nanoparticles on the catalytic oxidation of toluene over Pt/CeO$_2$ catalysts, Appl. Catal. B: Environ. 220 (2018) 462–470.

[27] T. Szumełda, A. Drelinkiewicz, E. Lalik, R. Kosydar, D. Duraczyńska, J. Gurgul, Carbon-supported Pd$_{100-x}$Au$_x$ alloy nanoparticles for the electrocatalytic oxidation of formic acid: influence of metal particles composition on activity enhancement, Appl. Catal. B: Environ. 221 (2018) 393–405.

[28] A. Davó-Quiñonero, D. Lozano-Castelló, A. Bueno-López, Unexpected stability of CuO/cryptomelane catalyst under preferential oxidation of CO reaction conditions in the presence of CO$_2$ and H$_2$O, Appl. Catal. B: Environ. 217 (2017) 459–465.

[29] Z. Li, C. Xiao, S. Fan, Y. Deng, W. Zhang, B. Ye, Y. Xie, Dual vacancies: an effective strategy realizing synergistic optimization of thermoelectric property in BiCuSeO, J. Am. Chem. Soc. 137 (2015) 6587–6593.

[30] H. Liu, Y. Zheng, G. Wang, S.Z. Qiao, A three-component nanocomposite with synergistic reactivity for oxygen reduction reaction in alkaline solution, Adv. Energy Mater. 5 (2015) 1401186.

[31] D. LeBoeuf, C.W. Rischau, G. Seyfarth, R. Küchler, M. Berben, S. Wiedmann, W. Tabis, M. Frachet, K. Behnia, B. Fauqué, Thermodynamic signatures of the field-induced states of graphite, Nat. Commun. 8 (2017) 1337.

[32] A.N. Soon, B.H. Hameed, Heterogeneous catalytic treatment of synthetic dyes in aqueous media using Fenton and photo-assisted Fenton process, Desalination 269 (2011) 1–16.

[33] S.V.L. Mahlaba, J. Valand, A.S. Mahomed, H.B. Friedrich, A study on the deactivation and reactivation of a Ni/Al$_2$O$_3$ aldehyde hydrogenation catalyst: effects of regeneration on the activity and properties of the catalyst, Appl. Catal. B: Environ. 224 (2018) 295–304.

[34] G. Hou, B. Cheng, Y. Cao, M. Yao, F. Ding, P. Hua, F. Yuan, Scalable synthesis of highly dispersed silicon nanospheres by RF thermal plasma and their use as anode materials for high-performance Li-ion batteries, J. Mater. Chem. A 3 (2015) 18136–18145.

[35] M. Yao, Q. Li, G. Hou, C. Lu, B. Cheng, K. Wu, G. Xu, F. Yuan, F. Ding, Y. Chen, Dopant-controlled morphology evolution of WO$_3$ polyhedra synthesized by RF thermal plasma and their sensing properties, ACS Appl. Mater. Interfaces 7 (2015) 2856–2866.

[36] G. Hou, B. Cheng, F. Ding, M. Yao, P. Hu, F. Yuan, Synthesis of uniform α-Si$_3$N$_4$ nanospheres by RF induction thermal plasma and their application in high thermal conductive nanocomposites, ACS Appl. Mater. Interfaces 7 (2015) 2873–2881.

[37] H. Zhang, T. Cao, Y. Cheng, Preparation of few-layer graphene nanosheets by radio-frequency induction thermal plasma, Carbon 86 (2015) 38–45.

[38] X.H. Wang, J.-G. Li, H. Kamiyama, M. Katada, N. Ohashi, Y. Moriyoshi, T. Ishigaki, Pyrogenic iron(III)-doped TiO$_2$ nanopowders synthesized in RF thermal plasma:

phase formation, defect structure, band gap, and magnetic properties, J. Am. Chem. Soc. 127 (2005) 10982–10990.

[39] S. Choi, T. Kim, H. Ji, H.J. Lee, M. Oh, Isotropic and anisotropic growth of metal-organic framework (MOF) on MOF: logical inference on MOF structure based on growth behavior and morphological feature, J. Am. Chem. Soc. 138 (2016) 14434–14440.

[40] D. Deng, L. Yu, X. Chen, G. Wang, L. Jin, X. Pan, J. Deng, G. Sun, X. Bao, Iron encapsulated within pod-like carbon nanotubes for oxygen reduction reaction, Angew. Chem. Int. Ed. 52 (2013) 371–375.

[41] J. Deng, P. Ren, D. Deng, X. Bao, Enhanced electron penetration through an ultrathin graphene layer for highly efficient catalysis of the hydrogen evolution reaction, Angew. Chem. Int. Ed. 54 (2015) 2100–2104.

[42] L. Gao, Q. Fu, M. Wei, Y. Zhu, Q. Liu, E. Crumlin, Z. Liu, X. Bao, Enhanced nickel-catalyzed methanation confined under hexagonal boron nitride shells, ACS Catal. 6 (2016) 6814–6822.

[43] A. Bhaskar, M. Deepa, T.N. Rao, MoO$_2$/multiwalled carbon nanotubes (MWCNT) hybrid for use as a Li-ion battery anode, ACS Appl. Mater. Interfaces 5 (2013) 2555–2566.

[44] D.V. Pham, R.A. Patil, C.-C. Yang, W.-C. Yeh, Y. Liou, Y.-R. Ma, Impact of the crystal phase and 3d-valence conversion on the capacitive performance of one-dimensional MoO$_2$, MoO$_3$, and Magnéli-phase Mo$_4$O$_{11}$ nanorod-based pseudocapacitorsh, Nano Energy 47 (2018) 105–114.

[45] S. Shah, O.G. Marin-Flores, K. Chinnathambi, M.G. Norton, S. Ha, Partial oxidation of surrogate Jet-A fuel over SiO$_2$ supported MoO$_2$, Appl. Catal. B: Environ. 193 (2016) 133–140.

[46] F. Li, L. Zhang, C. Hu, X. Xing, B. Yan, Y. Gao, L. Zhou, Enhanced azo dye decolorization through charge transmission by σ-Sb3$^+$-azo complexes on amorphous Sb$_2$S$_3$ under visible light irradiation, Appl. Catal. B: Environ. 240 (2019) 132–140.

[47] J. Liu, Q. Jia, J. Long, X. Wang, Z. Gao, Q. Gu, Amorphous NiO as co-catalyst for enhanced visible-light-driven hydrogen generation over g-C$_3$N$_4$ photocatalyst, Appl. Catal. B: Environ. 222 (2018) 35–43.

[48] Z. Jia, J. Kang, W.C. Zhang, W.M. Wang, C. Yang, H. Sun, D. Habibi, L.C. Zhang, Surface aging behaviour of Fe-based amorphous alloys as catalysts during heterogeneous photo Fenton-like process for water treatment, Appl. Catal. B: Environ. 204 (2017) 537–547.

[49] D. Zheng, H. Feng, X. Zhang, X. He, Yu M, X. Lu, Y. Tong, Porous MoO$_2$ nanowires as stable and high-rate negative electrodes for electrochemical capacitors, Chem. Commun. 53 (2017) 3929–3932.

[50] H. Shi, N. Poudel, B. Hou, L. Shen, J. Chen, A.V. Benderskii, S.B. Cronin, Sensing local pH and ion concentration at graphene electrode surfaces using in situ Raman spectroscopy, Nanoscale 10 (2018) 2398–2403.

[51] K. Im, H. Choi, K.S. Yoo, J. Kim, Synthesis of Ni promoted molybdenum dioxide nanoparticles using solvothermal cracking process for catalytic partial oxidation of n-dodecane, Korean J. Chem. Eng. 35 (2018) 283–288.

[52] S. Gu, M. Qin, H. Zhang, J. Ma, X. Qu, Preparation of Mo nanopowders through hydrogen reduction of a combustion synthesized foam-like MoO$_2$ precursor, Int. J. Refract. Met. Hard Mater. 76 (2018) 90–98.

[53] R. Nava, R.A. Ortega, G. Alonso, C. Ornelas, B. Pawelec, J.L.G. Fierro, CoMo/Ti-SBA-15 catalysts for dibenzothiophene desulfurization, Catal. Today 127 (2007) 70–84.

[54] Y. Pang, A. Zhong, Z. Xu, W. Jiang, L. Gu, X. Feng, W. Ji, C.-T. Au, How do core-shell structure features impact on the activity/stability of the Co-based catalyst in dry reforming of methane? ChemCatChem 10 (2018) 2845–2857.

[55] C.P. Jiménez-Gómez, J.A. Cecilia, R. Moreno-Tost, P. Maireles-Torres, Selective furfural hydrogenation to furfuryl alcohol using Cu-based catalysts supported on clay minerals, Top. Catal. 60 (2017) 1040–1053.

[56] H. Du, H. Zhu, Z. Zhao, W. Dong, W. Luo, W. Lu, M. Jiang, T. Liu, Y. Ding, Effects of impregnation strategy on structure and performance of bimetallic CoFe/AC catalysts for higher alcohols synthesis from syngas, Appl. Catal. A: Gen 523 (2016) 263–271.

[57] C. Zhang, X. Zou, Z. Du, J. Gu, S. Li, B. Li, S. Yang, Atomic layers of MoO$_2$ with exposed high-energy (010) facets for efficient oxygen reduction, Small 14 (2018) 1703960.

[58] G. Zhang, T. Xiong, M. Yan, L. He, X. Liao, C. He, C. Yin, H. Zhang, L. Mai, α-MoO$_{3-x}$ by plasma etching with improved capacity and stabilized structure for lithium storage, Nano Energy 49 (2018) 555–563.

[59] X. Luo, Y. Hong, F. Wang, S. Hao, C. Pang, E. Lester, T. Wu, Development of nano Ni$_x$Mg$_y$O solid solutions with outstanding anti-carbon deposition capability for the steam reforming of methanol, Appl. Catal. B: Environ. 194 (2016) 84–97.

[60] R. Xu, Y. Li, Z. Cao, J. Zheng, N. Zhang, B. Chen, W. Wang, Higher alcohol synthesis from syngas over KCoMoP catalysts, Catal. Commun. 51 (2014) 63–67.

[61] C. Dong, X. Li, A. Wang, Y. Chen, H. Liu, Influence of nanoscale distribution of Pd particles in the mesopores of MCM-41 on the catalytic performance of Pd/MCM-41, Catal. Commun. 100 (2017) 219–222.

[62] E.A. Permyakov, V.S. Dorokhov, V.V. Maximov, P.A. Nikulshin, A.A. Pimerzin, V.M. Kogan, Computational and experimental study of the second metal effect on the structure and properties of bi-metallic MeMoS-sites in transition metal sulfide catalysts, Catal. Today 305 (2018) 19–27.

[63] M. Liu, G. Fan, J. Yu, L. Yang, F. Li, Defect-rich Ni-Ti layered double hydroxide as a highly efficient support of Au nanoparticles for base-free and solvent-free selective oxidation of benzyl alcohol, Dalton Trans. 47 (2018) 5226–5235.

[64] M. Ao, G.H. Pham, J. Sunarso, M.O. Tade, S. Liu, Active centers of catalysts for higher alcohol synthesis from syngas: a review, ACS Catal. 8 (2018) 7025–7050.

[65] Y. Gao, L. Mi, W. Wei, S. Cui, Z. Zheng, H. Hou, W. Chen, Double metal ions synergistic effect in hierarchical multiple sulfide microflowers for enhanced supercapacitor performance, ACS Appl. Mater. Interfaces 7 (2015) 4311–4319.

[66] M. Tahir, Synergistic effect in MMT-dispersed Au/TiO$_2$ monolithic nanocatalyst for plasmon-absorption and metallic interband transitions dynamic CO$_2$ photo-reduction to CO, Appl. Catal. B: Environ. 219 (2017) 329–343.

[67] T.-H. Lu, C.-J. Chen, Y.-R. Lu, C.-L. Dong, R.-S. Liu, Synergistic-effect-controlled CoTe$_2$/carbon nanotube hybrid material for efficient water oxidation, J. Phys. Chem. C 120 (2016) 28093–28099.

[68] C.-H. Liu, R.-H. Liu, Q.-J. Sun, J.-B. Chang, X. Gao, Y. Liu, S.-T. Lee, Z.-H. Kang, S.-D. Wang, Controlled synthesis and synergistic effects of graphene-supported PdAu bimetallic nanoparticles with tunable catalytic properties, Nanoscale 7 (2015) 6356–6362.

[69] J. Hou, Y. Sun, Z. Li, B. Zhang, S. Cao, Y. Wu, Z. Gao, L. Sun, Electrical behavior and electron transfer modulation of nickel-copper nanoalloys confined in nickel-copper nitrides nanowires array encapsulated in nitrogen-doped carbon framework as robust bifunctional electrocatalyst for overall water splitting, Adv. Funct. Mater. 28 (2018) 1803278.

[70] N. Wang, J. Li, X. Liu, R. Hu, Y. Zhang, H. Su, X. Gu, Remarkable enhancement of the catalytic performance of molybdenum sulfide catalysts via an in situ decomposition method for higher alcohol synthesis from syngas, RSC Adv. 6 (2016) 112356–112362.

[71] W. Tang, Y. Deng, W. Li, J. Li, G. Liu, S. Li, X. Wu, Y. Chen, Importance of porous structure and synergistic effect on the catalytic oxidation activities over hierarchical Mn-Ni composite oxides, Catal. Sci. Technol. 6 (2016) 1710–1718.